Journal of Power Sources 196 (2011) 10010–10018

Contents lists available at ScienceDirect

Journal of Power Sources

journal homepage: www.elsevier.com/locate/jpowsour

Gas transport and internal-reforming chemistry in Ni–YSZ and ferritic-steel supports for solid-oxide fuel cells

Amy E. Richards, Michael G. McNeeley, Robert J. Kee, Neal P. Sullivan*

Engineering Division, Colorado School of Mines, Golden, CO 80401, USA

ARTICLE INFO

Article history:
Received 2 June 2011
Received in revised form 29 July 2011
Accepted 30 July 2011
Available online 4 August 2011

Keywords:
SOFC
Anode
Ni–YSZ
Metal support
AFL

ABSTRACT

Analyses of gas transport and hydrocarbon internal-reforming chemistry in nickel/yttria-stabilized zirconia (Ni–YSZ) and ferritic-steel supports for solid-oxide fuel cell applications are presented. The Ni–YSZ anode supports are fabricated using reaction-sintered powders (Ni–YRSZ) developed by CoorsTek, Inc. (Golden, CO, USA); the porous ferritic-steel supports are developed by PLANSEE SE (Reutte, Austria). The gas-transport and methane internal-reforming properties of these supports are measured using a unique "Separated Anode Experiment" that decouples these processes from electrochemical processes that are normally present in an operational SOFC. Experimental results are interpreted using a computational model. Despite significant differences in thickness and morphology between the Ni–YRSZ and ferritic-steel supports, results show that the rate of gas transport across the ferritic-steel support is comparable to that of the Ni–YRSZ support. While the Ni–YRSZ supports show extensive methane internal-reforming activity, the ferritic-steel supports are essentially inert towards methane reforming. This lack of internal-reforming activity in the metallic support motivates application of the computational model toward design of a Ni–YSZ anode-functional layer (AFL) to be placed atop the metallic support. Anode functional layers are found to provide a moderate level of internal reforming, though significantly lower than the complete Ni–YRSZ anode support, with very little effect on gas transport. The tools and methods presented here may be used for further design optimization of next-generation SOFC supports and architectures.

1. Introduction

Solid-oxide fuel cells can convert a broad range of hydrocarbon and biomass fuel sources into electricity. However, the threat of carbon-deposit formation and subsequent catalyst deactivation limits the robustness of SOFC operating windows. SOFC developers are taking many approaches in creating solutions to these problems, such as the barrier-layer work of the Barnett group [1], the copper–ceria anodes developed by Gorte and colleagues [2], and the perovskite anodes developed by Irvine [3] and Barnett [4], to name a few. More recently, developments have included metal-supported SOFCs with thin anode-functional layers [5,6]. While all of these approaches show great promise, the gas-transport and hydrocarbon internal-reforming processes within these materials and structures are not well understood.

Traditional electrochemical testing methods, such as polarization measurements and electrochemical impedance spectroscopy, provide valuable information on cell performance. However, as these techniques are conducted on complete operational cells, anode-specific processes can be masked by other electrochemical processes. The "Separated Anode Experiment" enables focus on gas transport and internal-reforming chemistry within the anode support by decoupling these processes from electrochemical phenomena. In this study, this experiment is configured to examine and compare the gas-transport and internal-reforming characteristics of a porous ferritic-steel support with those of a more-conventional support comprised of nickel and yttria-stabilized zirconia (Ni–YSZ). The ferritic steel support is fabricated by PLANSEE SE (Reutte, Austria), while the Ni–YSZ support is fabricated using powders provided by CoorsTek, Inc. (Golden, Colorado, USA). Interpretation of experimental results is aided by a detailed computational model. The model also provides insight to design of anode functional layers for enhancing internal-reforming performance.

1.1. Metal-supported cells

Metal supports have many potential advantages over Ni–YSZ anode supports, including decreased materials and fabrication costs, mechanical toughness, and thermal-cycling durability [7]. Many materials have been investigated for use as metal supports, and are typically either nickel [5,8–10] or iron based [5,6,8–14]. Cho et al. [15] and Hwang et al. [16] have developed SOFCs supported on

* Corresponding author. Tel.: +1 303 273 3656; fax: +1 303 273 3602.
E-mail address: nsulliva@mines.edu (N.P. Sullivan).

0378-7753/$ – see front matter © 2011 Elsevier B.V. All rights reserved.
doi:10.1016/j.jpowsour.2011.07.086

porous Ni substrates. These supports demonstrated high catalytic activity for internal reforming of hydrocarbon fuels, but were susceptible to carbon deposition and sulfur poisoning, like traditional Ni–YSZ supports. Additionally, the thermal-expansion behavior of the nickel support is not well matched to that of typical ceramic electrolyte materials, and can lead to cell-fabrication problems.

Nickel–iron alloys are also being explored [5,9,10,12,17], including 300-series austenitic and 400-series ferritic stainless steels. In an evaluation of 316L porous stainless steel, Molin et al. [17] demonstrate that a non-conductive Fe–Cr oxide scale can form at typical SOFC temperatures, negatively affecting SOFC performance. A significant thermal-expansion mismatch also exists between 300-series steels and common SOFC electrolytes [5].

Ferritic stainless steels are receiving significant interest as interconnects for SOFC stacks [7], and as SOFC supports [6,18]. These materials typically contain between 10 wt.% and 26 wt.% Cr, which promotes formation of an electronically conductive continuous chromia scale under SOFC operating conditions. Thermal expansion is similar to that of SOFC electrolytes [5]. Additionally, ferritic steels are relatively inexpensive, with well-established industrial-fabrication processes. Rivas et al. reported on the performance of Crofer22APU as a porous metal support [12]. Oxidation rates were found to be unacceptably high; the study concludes that the material is currently incapable of meeting lifetime demands for a porous metal support.

PLANSEE SE has developed a ferritic steel for intermediate-temperature SOFC applications [6,18], termed "ITM" alloy. This material contains 26% Cr, with trace levels of Mo, Ti, and Y_2O_3, balanced by Fe. The metal oxides improve the mechanical strength and creep resistance of the alloy, while additional alloying elements adapt physical (i.e. thermal expansion, mechanical strength) and chemical (i.e. corrosion) properties to SOFC applications. The ITM alloy is fabricated using powder-metallurgy processing, resulting in a more-homogenous element distribution, and formation of a well-adhered protective-oxide scale during cell operation.

The differences in the composition and morphology of these support materials clearly impact cell performance. However, gas transport and hydrocarbon internal-reforming chemistry within metallic supports are not well understood. In this study, experimental and numerical tools are used to examine and compare the gas-transport and internal-reforming behavior of traditional Ni–YSZ anodes with that of porous ferritic-steel supports.

2. Experimental methods

2.1. Materials

The benchmark SOFC support for this study is formulated from the reaction-sintered Ni–YSZ (Ni–YRSZ) anode powders developed by CoorsTek, Inc. [19,20]. Powder preparation begins by combining and ball-milling 92 mol% monoclinic zirconia powder with 8 mol% yttria powder. The yttria–zirconia powder is dried and screened, then blended with 65 wt.% nickel oxide. The NiO powders have a particle size of approximately 10 μm. The NiO, Y_2O_3, and ZrO_2 powders are then mixed with a binder solution to form a slurry; no pore former is added. The slurry is spray-dried into a rotary atomizer.

Following drying, powders are weighed into 5- or 10-g portions and pressed into disc-shaped powder compacts within a 5.715 cm (2.25 in.) diameter stainless steel die using a uni-axial press (Carver AutoFour30) loaded to 53.4 kN (12,000 lb) with a 10 s hold time. Compacts are transferred from the die onto YSZ–Al_2O_3 porous setter plates (Selee Ceramics) and sintered in air at a temperature of 1450–1550 °C for 4 h. After sintering, Ni–YRSZ anode supports measure approximately 4.43 cm (1.74 in.) in diameter and 0.79 or 1.45 mm in thickness for the 5- and 10-g samples, respectively. Due to the open pore structure of the CoorsTek Ni–YRSZ material, this anode support has demonstrated exceptionally high gas transport and catalytic activity for hydrocarbon fuels [19].

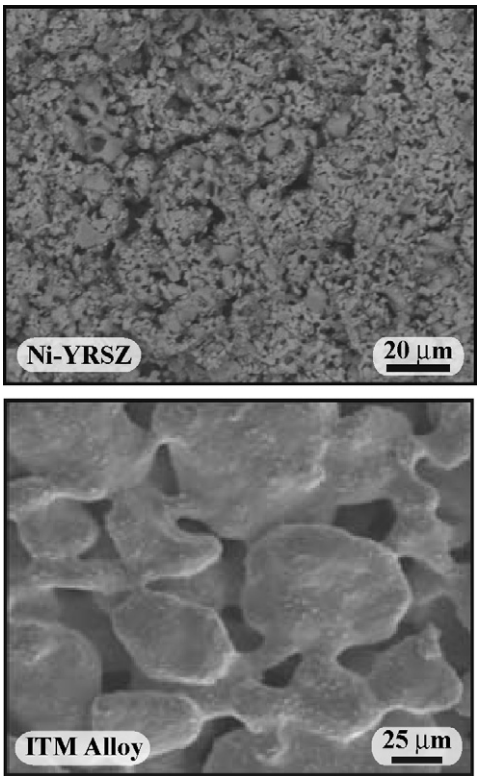

Fig. 1. SEM images of (a) Ni–YRSZ anode and (b) ferritic steel supports.

The porous metal support provided by PLANSEE SE is 1 mm thick, with the composition described previously [18].

2.2. Support characterization

In addition to material composition, morphological properties of the anode supports have a great effect on the gas-transport and internal-reforming behavior. Several methods of characterization are performed to gain an understanding of the physical form of the support structures. For broad visualization, electron-microscopy images of support surfaces are taken using a JEOL JSM-7000F Field Emission Scanning Electron Microscope. Prior to SEM analysis, the Ni–YRSZ anodes are exposed to a reducing environment of forming gas (3.5% H_2, balance N_2) at 800 °C for at least 48 h. Fig. 1 shows significant differences in support microstructure, with particle and pore sizes of the metal support found to be much larger than those of the Ni–YRSZ material. These qualitative differences are quantified through additional characterization.

Porosity is determined using liquid picnometry (Archimedes' method), and pore-size distribution is obtained via mercury porosimetry (Micromeritics Particle Analysis, Norcross, GA, USA), with results provided in Table 1. The open porosity of the two mate-

Table 1
Morphological properties of Ni–YRSZ and metallic supports.

Property	Ni–YRSZ	ITM alloy
Porosity	41%	41.7%
Mean pore radius (μm)	0.9	8.6
Mean particle diameter (μm)	1.0	65
Catalyst surface area (m^{-1})	150,000	0
Thickness (mm)	1.45	1.0
Tortuosity	5.8	10.1

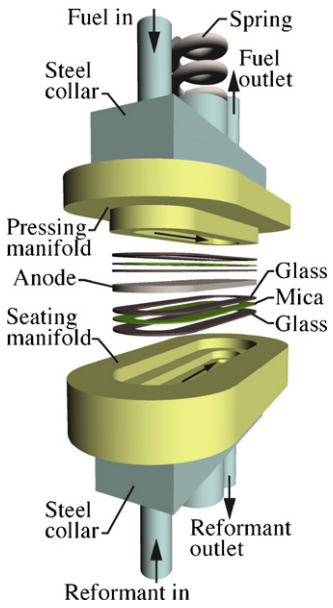

Fig. 2. Illustration of the Separated Anode Experiment.

rials is found to be very similar (~41%). As evidenced in the images of Fig. 1, the pore radius and particle diameter of the PLANSEE ITM alloy is over an order of magnitude greater than that of the CoorsTek Ni–YRSZ support. The tortuosity and catalyst specific surface area reported in the table are not directly measured. Rather, they are quantified as computational fitting parameters to experimental results, as explained subsequently.

2.3. Separated Anode Experiment

The Separated Anode Experiment (SAE) has been developed to decouple gas transport and hydrocarbon internal-reforming chemistry from SOFC electrochemistry (Fig. 2) [21]. A planar support is placed within alumina pressing and seating manifolds into which flow channels have been machined. The flow channels are 28.96 mm (1.14 in.) long, 6.35 mm (0.25 in.) wide, and 2.54 mm (0.1 in.) high. The support is sealed within the manifolds using 0.6 mm thick mica sandwiched between two pieces of glass filter paper (Fisher Scientific, G6). Upon heating, the glass melts to fill voids in the mica surface. The manifold-support assembly is compressed within a furnace and is heated to 800 °C for all experiments.

Anode supports containing Ni are reduced under a mixture of hydrogen and nitrogen for at least 48 h prior to testing. The fuel channel (top) is fed with gases representative of SOFC fuel streams (CH_4, biogas, and higher hydrocarbons). The electrolyte channel (bottom) is fed with gases that would be generated at triple-phase boundaries (steam and CO_2). Both fuel- and electrolyte-gas compositions are diluted with forming gas (3.5% H_2, balance N_2). The H_2 serves to prevent nickel oxidation while the N_2 acts a diluent to prevent carbon-deposit formation. Visual inspection of supports following testing reveals no carbon-deposit formation.

Gases from the fuel and electrolyte channels cross-diffuse through the porous support and participate in heterogeneous reforming reactions. The composition of the exhaust streams from each channel is measured with a gas chromatograph (Agilent MicroGC 3000 equipped with molecular-sieve and Plot-U columns) and used to infer the gas transport and heterogeneous chemistry underway within the porous support structure. Alumina manifolds and tubing prevent surface reactions anywhere other than the support under test. Experiments are performed over a range of flow rates spanning 75–200 mL min^{-1}, keeping internal-reforming chemistry within the kinetic regime.

Initial gas-transport tests measure the diffusion of a near-inert gas across the porous support structure. The fuel channel is supplied with 100% forming gas (FG) while the electrolyte channel is supplied with a mixture of 50% FG and 50% CO_2. The fuel-channel exhaust composition indicates the amount of CO_2 diffusing through the support from the electrolyte channel. Through this experiment, a comparison of gas-transport behavior is made between the Ni–YRSZ and ITM ferritic-steel supports.

Methane internal-reforming experiments utilize a mixture of 20% CH_4/80% FG in the fuel channel and a 50% CO_2/50% FG mixture in the electrolyte channel. The exhaust-gas compositions of both the fuel and electrolyte channels are measured as flow rate is increased from 75 to 200 mL min^{-1}. While steam is the direct product of electrochemistry, CO_2 is used in lieu of H_2O in an effort to improve experimental repeatability and control. CO_2 ("dry") reforming clearly results in significantly different product compositions in comparison to steam reforming. However, Rostrup-Nielsen and Hansen show that the kinetics of the methane steam- and dry-reforming reactions over a nickel catalyst are quite similar [22]. Due to the simplicity and improved experimental control, dry-reforming experiments have been found most effective for the purposes of comparing methane internal-reforming activity across different support materials and structures. Each set of measurements is repeated three times at each flow rate tested; experimental repeatability is found to be very good.

3. Computational model

A computational model has been developed to simulate the gas transport and chemical processes occurring within the support structures. Fig. 3 shows an illustration of this model. Flow within the fuel and electrolyte channels is described using a series of perfectly stirred tank reactors in which axial variations (x-direction) are captured, but perfect mixing is assumed throughout the channel cross section (y and z directions). Flow within the porous support structure is described using the Dusty-Gas Model [23,24], in which transport due to axial gradients within the porous support is considered negligible in comparison to that caused by gradients in the z-direction.

3.1. Flow in channels

Each separate control volume of the flow channel is treated as a perfectly stirred tank reactor. Temperature and composition within the reactor are taken to be uniform [25]. The species continuity equation for flow within the fuel channel is:

$$\dot{m}_k^* = \dot{m}_k + j_k^c A_c, \tag{1}$$

where $\dot{m}_k^*$ and $\dot{m}_k$ are the mass flow rates in and out, respectively, of the channel element in the x-direction, j_k^c is the mass flux of species k in the z-direction from the channel into the support, and A_c is the cross-sectional area between the fuel channel and support control volume. The continuity equation within the fuel channel is:

$$\dot{m}^* = \dot{m} + \sum_{k=1}^{K} j_k^c A_c, \tag{2}$$

where K is the number of total species and

$$\dot{m}_k = Y_k \dot{m}, \tag{3}$$

Y_k represents the mass fraction of species k. Within the flow channels, gas-phase chemistry is assumed to be negligible in comparison to catalytic chemistry on the support surface. At temperatures

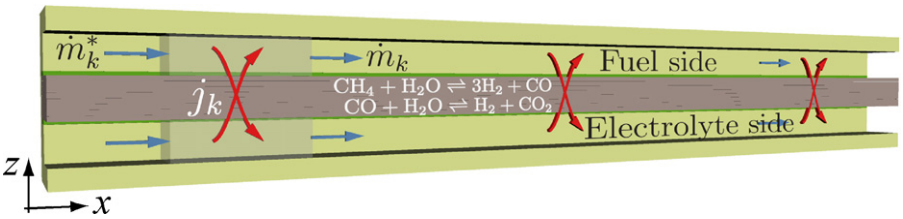

Fig. 3. An illustration of the framework represented by the computational model.

around 800 °C and lower, methane pyrolysis is kinetically very slow. For the short residence times under these experimental conditions (0.28–0.75 s), it has been shown that neglecting gas-phase chemistry is a very reasonable assumption [26]. Since the pore size within the support is comparable to the molecular mean-free-path length, the probability for gas–gas collisions is low. Gas-phase chemistry within the voids of the support can therefore be neglected [21].

3.2. Transport and chemistry within the porous support

The gas composition within the support is determined by solving a reactive porous-media problem. The species continuity equation within the support is

$$\frac{\partial j_k}{\partial z} = \dot{s}_k W_k A_s, \tag{4}$$

where j_k is the z-component of the mass flux of species k within the anode, A_s is the specific area (i.e., area per unit volume) of the exposed nickel catalyst, $\dot{s}_k$ is the net molar production rate of gas-phase species k by heterogeneous reforming chemistry, and W_k are the species molecular weights [27]. The mass-continuity equation within the anode is,

$$\sum_{k=1}^{K} \frac{\partial j_k}{\partial z} = \sum_{k=1}^{K} \dot{s}_k W_k A_s. \tag{5}$$

Species fluxes in the z-direction within the porous catalyst are governed by the Dusty-Gas Model (DGM), which is an implicit relationship between the gas-phase species molar fluxes j_k, molar concentrations $[X_k]$, concentration gradients, and the pressure gradient p as

$$\sum_{\ell \neq k} \frac{[X_\ell] j_k - [X_k] j_\ell}{[X_T] D^e_{k\ell}} + \frac{j_k}{D^e_{k,Kn}} = -\frac{\partial X_k}{\partial z} - \frac{[X_k]}{D^e_{k,Kn}} \frac{B_g}{\mu} \frac{\partial p}{\partial z}. \tag{6}$$

Here, X_T is the total molar concentration, B_g is the permeability, and μ is the mixture viscosity. The ordinary diffusion coefficient $D^e_{k\ell}$ and the Knudsen diffusion coefficient $D^e_{k,Kn}$ depend on the binary gas-to-gas diffusion coefficients (evaluated from kinetic theory) and on the physical porous-media properties.

The effective molecular binary diffusion coefficients in the porous media are related to bulk-phase ordinary diffusion coefficients as

$$D^e_{k\ell} = \frac{\phi_g}{\tau_g} D_{k\ell}, \tag{7}$$

where ϕ_g is the material porosity and τ_g is tortuosity. Knudsen diffusion, which occurs due to gas–wall collisions, becomes dominant when the mean-free path of the molecular species is much larger than the pore diameter. The effective Knudsen diffusion coefficient is expressed as

$$D^e_{k,Kn} = \frac{4}{3} K_g \sqrt{\frac{8RT}{\pi W_k}}, \tag{8}$$

where the Knudsen permeability coefficient $K_g = r_p \phi_g / \tau_g$, and r_p is the average pore radius. Assuming that the porous electrode is formed by closely packed spherical particles with diameter d_p, the permeability B_g can be expressed by the Kozeny-Carman relationship [28] as

$$B_g = \frac{\phi_g^3 d_p^2}{72 \tau_g (1 - \phi_g)^2}. \tag{9}$$

During SOFC operation, the differential pressure between the fuel channel and the triple-phase boundaries is quite low (~1000 Pa) [29]. In an effort to reproduce SOFC conditions, great care is taken during Separated Anode testing to equilibrate the pressures on either side of the support. This minimizes pressure-driven flow across the support, so that the species-concentration gradients are the driving forces for gas transport in these experiments.

Heterogeneous chemistry within the anode is represented by an elementary reaction mechanism describing CH_4 reforming on Ni-based catalysts. This kinetic mechanism is taken from Hecht et al. [21] and contains 42 irreversible elementary reactions (see Table 2) involving six gas-phase and twelve surface-adsorbed species. Unlike global reaction mechanisms, this mechanism is based on elementary molecular processes, and is developed from a combination of kinetic theory and experimentation. It represents all global chemical processes for methane reforming in a Ni–YSZ support, including steam reforming, partial oxidation, and dry reforming of CH_4 to CO and H_2, and water–gas-shift processes. Because all chemistry is represented as a set of elementary reactions, the mechanism can be used across a broad range of applications and reactant compositions. Details of kinetic-mechanism development can be found in Hecht et al. [21]

The series of nonlinear equations outlined above is solved computationally using the CANTERA software package [30]. CANTERA has been chosen for this application because of its versatility and suitability for solving chemically reacting flow problems. The species continuity equations for the fuel and electrolyte channels (Eq. (1)) are coupled to the species continuity equations for the support (Eq. (4)) via the mass fluxes j_k^c exchanged between the support and flow channels. The compositions at the top and bottom of the support are taken to be the compositions within the flow channels. It is assumed that there is no mass-transport resistance between the support and flow channels. A modified Newton method is used here as the solution algorithm, with the channels being divided into cells of length Δx and the support divided into cells of length Δz. The temperature is assumed to be uniform as set by the external furnace, and pressure is assumed to be atmospheric and equal in both flow channels. These assumptions have been validated with measurements. Channel flows are assumed isobaric.

4. Results and discussion

4.1. Ni–YRSZ anode support

4.1.1. CO_2 transport

Results from an analysis of the CoorsTek Ni–YRSZ support are first presented, with comparisons then made to results for the

Table 2
Heterogeneous reaction mechanism for CH_4 on Ni [21].

	Reaction	A [a]	E [a]
1.	$H_2 + Ni(s) + Ni(s) \rightarrow H(s) + H(s)$	1.000E−02 [b]	0.00
2.	$H(s) + H(s) \rightarrow Ni(s) + Ni(s) + H_2$	5.593E+19 [b]	88.12
3.	$O_2 + Ni(s) + Ni(s) \rightarrow O(s) + O(s)$	1.000E−02 [b]	0.00
4.	$O(s) + O(s) \rightarrow Ni(s) + Ni(s) + O_2$	2.508E+23 [b]	470.39
5.	$CH_4 + Ni(s) \rightarrow CH_4(s)$	8.000E−03 [b]	0.00
6.	$CH_4(s) \rightarrow Ni(s) + CH_4$	5.302E+15 [b]	33.15
7.	$H_2O + Ni(s) \rightarrow H_2O(s)$	1.000E−01 [b]	0.00
8.	$H_2O(s) \rightarrow Ni(s) + H_2O$	4.579E+12 [b]	62.68
9.	$CO_2 + Ni(s) \rightarrow CO_2(s)$	1.000E−05 [b]	0.00
10.	$CO_2(s) \rightarrow Ni(s) + CO_2$	9.334E+07 [b]	28.80
11.	$CO + Ni(s) \rightarrow CO(s)$	5.000E−01 [b]	0.00
12.	$CO(s) \rightarrow Ni(s) + CO$	4.041E+11 [b]	112.85
		$\varepsilon_{CO(s)}$	−50.0 [c]
13.	$O(s) + H(s) \rightarrow OH(s) + Ni(s)$	5.000E+22	97.90
14.	$OH(s) + Ni(s) \rightarrow O(s) + H(s)$	2.005E+21	37.19
15.	$OH(s) + H(s) \rightarrow H_2O(s) + Ni(s)$	3.000E+20	42.70
16.	$H_2O(s) + Ni(s) \rightarrow OH(s) + H(s)$	2.175E+21	91.36
17.	$OH(s) + OH(s) \rightarrow O(s) + H_2O(s)$	3.000E+21	100.00
18.	$O(s) + H_2O(s) \rightarrow OH(s) + OH(s)$	5.423E+23	209.37
19.	$O(s) + C(s) \rightarrow CO(s) + Ni(s)$	5.200E+23	148.10
20.	$CO(s) + Ni(s) \rightarrow O(s) + C(s)$	1.418E+22	115.97
		$\varepsilon_{CO(s)}$	−50.0 [c]
21.	$O(s) + CO(s) \rightarrow CO_2(s) + Ni(s)$	2.000E+19	123.60
		$\varepsilon_{CO(s)}$	−50.0 [c]
22.	$CO_2(s) + Ni(s) \rightarrow O(s) + CO(s)$	3.214E+23	86.50
23.	$HCO(s) + Ni(s) \rightarrow CO(s) + H(s)$	3.700E+21	0.0
		$\varepsilon_{CO(s)}$	−50.0 [c]
24.	$CO + H(s) \rightarrow HCO(s) + Ni(s)$	2.338E+20	127.98
25.	$HCO(s) + Ni(s) \rightarrow O(s) + CH(s)$	3.700E+24	95.80
26.	$O(s) + CH(s) \rightarrow HCO(s) + Ni(s)$	7.914E+20	114.22
27.	$CH_4(s) + Ni(s) \rightarrow CH_3(s) + H(s)$	3.700E+21	57.70
28.	$CH_3(s) + H(s) \rightarrow CH_4(s) + Ni(s)$	4.438E+21	58.83
29.	$CH_3(s) + Ni(s) \rightarrow CH_2(s) + H(s)$	3.700E+24	100.00
30.	$CH_2(s) + H(s) \rightarrow CH_3(s) + Ni(s)$	9.513E+22	52.58
31.	$CH_2(s) + Ni(s) \rightarrow CH(s) + H(s)$	3.700E+24	97.10
32.	$CH(s) + H(s) \rightarrow CH_2(s) + Ni(s)$	3.008E+24	76.43
33.	$CH(s) + Ni(s) \rightarrow C(s) + H(s)$	3.700E+21	18.80
34.	$C(s) + H(s) \rightarrow CH(s) + Ni(s)$	4.400E+22	160.49
35.	$O(s) + CH_4(s) \rightarrow CH_3(s) + OH(s)$	1.700E+24	88.30
36.	$CH_3(s) + OH(s) \rightarrow O(s) + CH_4(s)$	8.178E+22	28.72
37.	$O(s) + CH_3(s) \rightarrow CH_2(s) + OH(s)$	3.700E+24	130.10
38.	$CH_2(s) + OH(s) \rightarrow O(s) + CH_3(s)$	3.815E+21	21.97
39.	$O(s) + CH_2(s) \rightarrow CH(s) + OH(s)$	3.700E+24	126.80
40.	$CH(s) + OH(s) \rightarrow O(s) + CH_2(s)$	1.206E+23	45.42
41.	$O(s) + CH(s) \rightarrow C(s) + OH(s)$	3.700E+21	48.10
42.	$C(s) + OH(s) \rightarrow O(s) + CH(s)$	1.764E+21	129.08

[a] Arrhenius parameters for the rate constants written in the form: $k = A \exp(-E/RT)$. The units of A are given in terms of moles, centimeters, and seconds. E is in kJ/mol.
[b] Sticking coefficient.
[c] Coverage dependent activation energy. Detailed definition may be found in Hecht et al. [21]. Total available surface site density is $\Gamma = 2.60 \times 10^{-9}$ mol cm^{-2}.

PLANSEE ITM metallic support. CO_2 transport across the Ni–YRSZ support is shown in Fig. 4; experimental measurements are shown as symbols, while computational predictions are shown as lines. In these experiments, CO_2 fed to the electrolyte channel diffuses through the support into the fuel channel. As flow rates increase, residence times in the flow channels decrease, and the amount of CO_2 reaching the fuel channel goes down. Experimental repeatability is very good, with standard deviations that result in error bars that are approximately the same size as the symbols that are used to represent experimental data. For this reason, error bars are not included in these figures.

The tortuosity of the support is used as a fitting parameter to correlate experiment and model, and is set to a value of 5.8 for the CoorsTek Ni–YRSZ anode support (Table 1). This value is determined for a single flow rate, and is then held constant for the remaining transport and reforming simulations. Strong agreement is found between experimental results and model predictions.

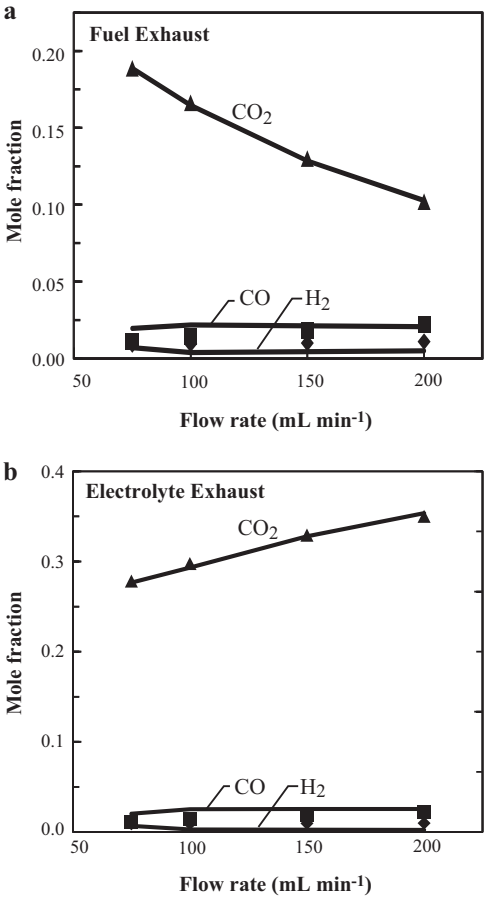

Fig. 4. Results for CO_2-transport experiments on a Ni–YRSZ support: exhaust-gas composition in (a) fuel-exhaust stream; and (b) electrolyte-exhaust stream. Experimental results are represented by symbols, while model results are shown as lines.

Some measure of catalytic activity is evident in these CO_2-transport experiments. If the CO_2 experiments were fully inert, hydrogen mole fraction would range between the 1.75% H_2 fed to the electrolyte channel and the 3.5% H_2 fed to the fuel channel. However, very little hydrogen (<1%) is found in the exhaust gases from either channel over all flow rates. Additionally, significant CO formation (~2%) is observed. These experimental results indicate the occurrence of the reverse water–gas shift ($CO_2 + H_2 \rightarrow CO + H_2O$), where CO_2 reacts with the small amount of H_2 present in the forming gas to produce steam and CO. Gas-transport tests are therefore not entirely inert. In order to accurately model the gas-transport tests, the heterogeneous chemistry must be included in these simulations, as has been done in the model results shown in Fig. 4.

The computational model can be probed to provide additional insight into the gas-transport processes within the Ni–YRSZ support. Fig. 5 shows a contour plot of the CO_2 diffusion within the support at the 75 mL min^{-1} flow-rate condition. The thickness of the anode support has been scaled by a factor of eight to enable better visualization of the CO_2 field across the porous structure. Again, CO_2 is introduced on the electrolyte side, and diffuses to the fuel side through the anode support. The CO_2-concentration field shows balanced diffusion across the anode structure, with higher gradients found near the inlets. While some reverse water–gas shift chemistry occurs under these conditions, the overall effect on the CO_2 concentration field is limited.

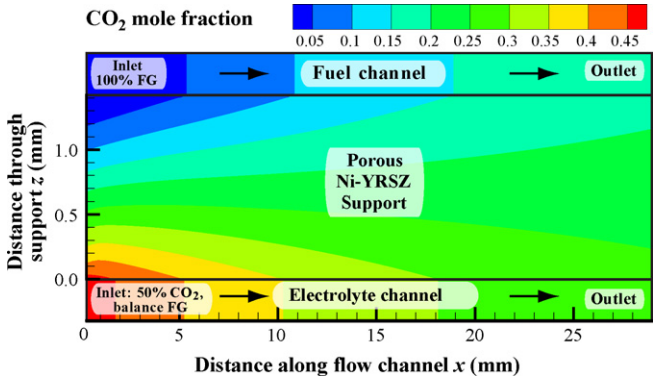

Fig. 5. Model-predicted CO_2-concentration field through the Ni–YRSZ support at the 75 mL min^{-1} flow rate. The support thickness (vertical direction) has been scaled by a factor of eight.

4.1.2. CH_4 dry reforming

After completion of CO_2 gas-transport experiments, CH_4 dry-reforming experiments are conducted. The fuel channel is fed with a 20:80 CH_4:forming-gas mixture, while the electrolyte channel is fed with a 50:50 CO_2:forming-gas mixture. Experimental and computational results are shown in Fig. 6. As in the transport results, experimental repeatability is very good, with error bars that are approximately the same size as the symbols that represent experimental data.

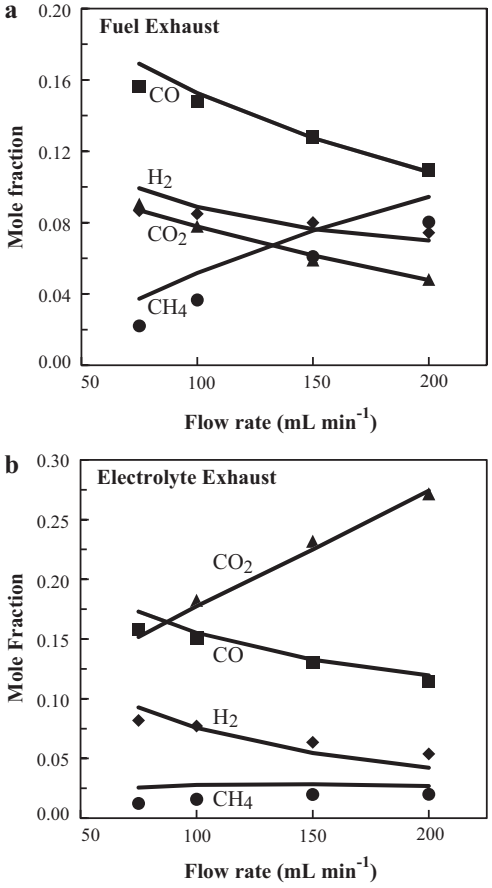

Fig. 6. Exhaust mole fractions from CH_4 dry-reforming experiments on the Ni–YRSZ anode support: gas composition of (a) fuel-exhaust stream; and (b) electrolyte-exhaust stream. Experimental results are represented by symbols, while model results are shown as lines.

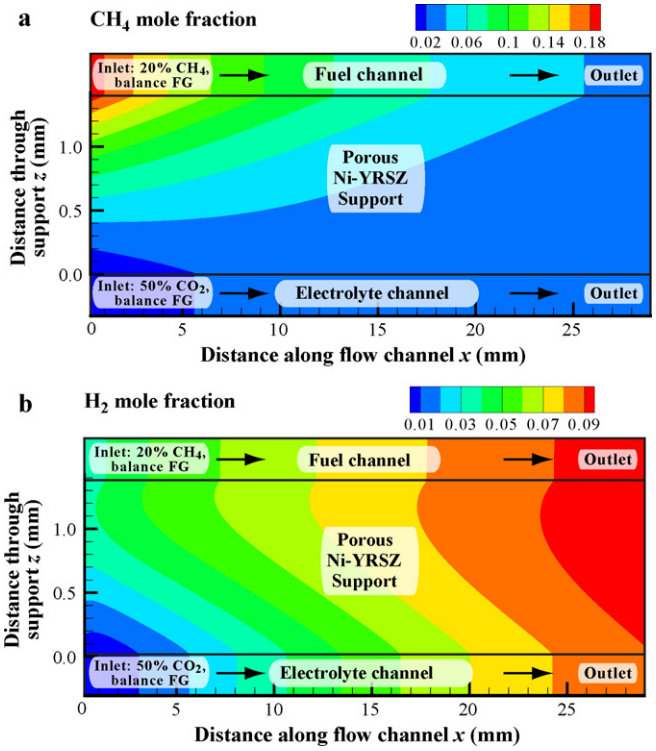

Fig. 7. Model-predicted species-concentration fields through the Ni–YRSZ support at the 75 mL min^{-1} flow rate: (a) CH_4 mole fraction; and (b) H_2 mole fraction. Note that the thickness of the anode support (vertical direction) has been scaled by a factor of eight.

Fig. 6 shows that the Ni–YRSZ anode is highly active for methane dry reforming. Reactant conversion and product formation is higher at the lower flow rates and longer residence times. The high hydrogen concentration (nearly 10% at longer residence times) and low methane concentration (<5%) in both exhaust streams indicate high catalytic activity of the CoorsTek anode support. A small amount (<3%) of CH_4 diffuses unreacted through the Ni–YRSZ support into the electrolyte channel, indicating that the chemistry does not reach equilibrium, and is kinetically limited. Analysis of the rates of production for the multiple reactions in the kinetic mechanism indicates that the rate-limiting step is the hydrogen abstraction from the surface-adsorbed CH_4, in keeping with the studies of Wei and Iglesia [31].

The model and experiment agree well for all species present, indicating that the kinetic model accurately captures the internal-reforming processes. Catalyst specific surface area is used as a model fitting parameter; once set, it is held constant for all flow rates. In this case, a value of 150,000 m^{-1} is used. The experimental hydrogen concentration profiles are somewhat flatter than those predicted by the model, possibly due to upstream diffusion of hydrogen at lower flow rates.

Fig. 7 illustrates diffusion and reforming processes within the anode at the 75 mL min^{-1} flow-rate condition. Composition fields vary significantly from those of the inert-diffusion case presented in Fig. 5 due to the coupled and competing effects of gas-transport and internal-reforming processes. For the long-residence-time condition shown, methane concentration (Fig. 7(a)) is low but non-zero through most of the support. Gradients are highest near the inlet. Higher H_2 concentrations (Fig. 7(b)) are found closer to the fuel channel, where CH_4 content is the highest. H_2 concentration increases steadily with axial position, indicating active reforming reactions throughout the length of the support. This H_2-field illustrates how internal reforming can enable better distribution of

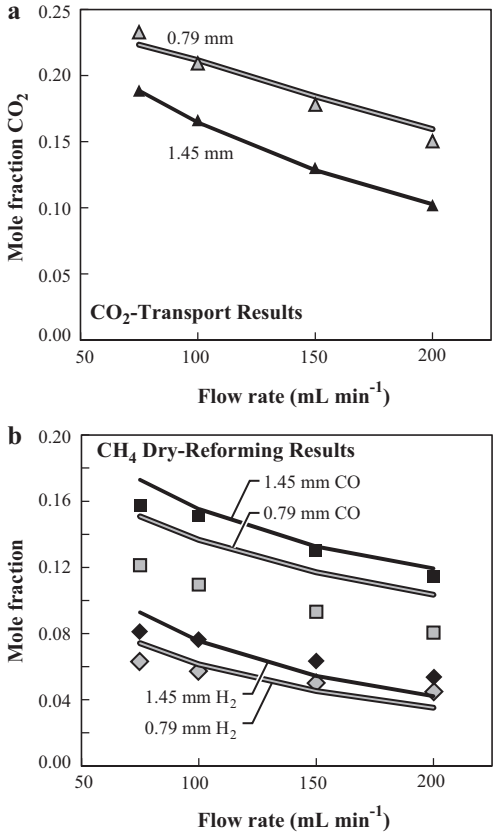

Fig. 8. Exhaust mole fractions from Separated Anode Experiments on Ni–YRSZ anodes of thickness 0.79 and 1.45 mm: (a) CO_2-transport results: CO_2 mole fraction in the fuel-exhaust stream; (b) CH_4 dry-reforming results: H_2 and CO mole fraction in electrolyte-exhaust stream. Experimental results are represented by symbols, and computational results by lines.

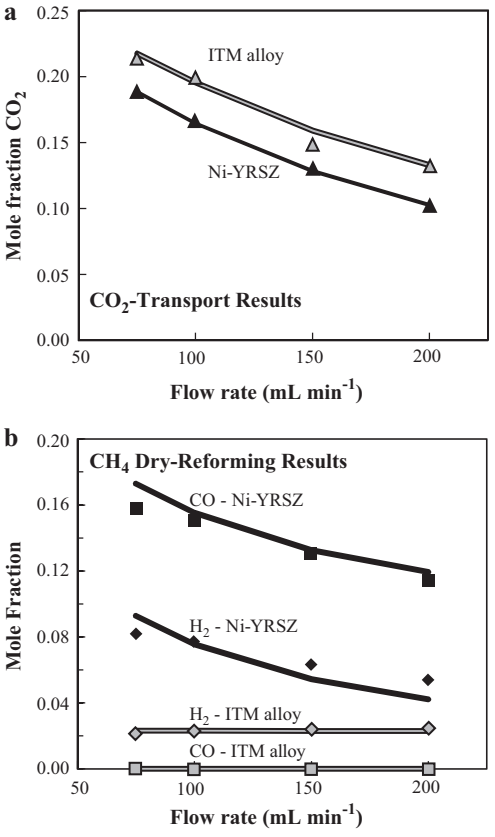

Fig. 9. Exhaust mole fractions from Separated Anode Experiments on Ni–YRSZ and porous-metal supports: (a) CO_2-transport results: mole fraction of CO_2 in fuel-exhaust stream; (b) CH_4 dry-reforming results: syngas mole fraction in the electrolyte-exhaust. Experimental results are represented by symbols, and model results by lines.

syngas and more-uniform current density across the length of an SOFC.

4.2. Effect of anode thickness

Species mass-transport rates through the porous support can be increased by reducing the support thickness. This also reduces the residence time of gases within the catalytically active support, potentially decreasing the extent of internal reforming. To study this further, CO_2-transport and CH_4 dry-reforming results are compared for CoorsTek Ni–YRSZ supports of 0.79-mm and 1.45-mm in thickness. Numerical simulations use identical physical properties for the two supports, including porosity, pore radius, tortuosity, and catalyst surface area (Table 1); the only difference is the support thickness.

CO_2-transport results are shown in Fig. 8(a), and dry-reforming results are shown in Fig. 8(b). The more-facile diffusion through the thinner anode results in a nearly 50% increase in CO_2 in the fuel-exhaust stream (Fig. 8(a)). However, the increased transport across the support does not result in greater syngas formation, with lower CO and H_2 concentrations found in the electrolyte exhaust of the thinner support (Fig. 8(b)). Higher methane concentrations are also observed in the electrolyte exhaust stream for the thinner support. This reduced syngas formation is indicative of the kinetic effects of internal reforming within the porous support structure. While increased gas transport is generally desirable in SOFC supports, adequate residence time within the structure is needed to achieve high methane conversion and syngas formation.

The agreements between model and experimental data are very good for transport of CO_2 (Fig. 8(a)), the conversion of CH_4 (not shown), and the selectivity to hydrogen (Fig. 8(b)). However, the model significantly overpredicts CO formation in the thinner support (Fig. 8(b)). Similarly, CO_2 (not shown) is under-predicted, which is consistent with a closed carbon balance. As the gas transport, methane conversion, and hydrogen selectivity appear to be well characterized, the inconsistencies in predicting CO and CO_2 species may speak to the limitations of the kinetic mechanism. The mechanism was initially developed and validated to describe steam-assisted catalytic partial oxidation of methane in small-channel monolith reactors using Ni supported on alumina [21]. The materials, reforming conditions, and geometries used in this study are clearly quite different from those for which this mechanism has been validated. YSZ itself also has catalytic activity for methane conversion [32], and may contribute to the differences observed in Fig. 8(b). Although the model and experimental data differ with regard to these species, the model-derived insight on SOFC internal-reforming processes and its dependence on anode-support structure is quite valuable.

4.3. Comparison of metallic and Ni–YRSZ supports

Fig. 9 shows a comparison of gas-transport and internal-reforming behavior of the PLANSEE ITM porous metal support to the 1.45-mm thick CoorsTek Ni–YRSZ support. The morphological properties used in computations are provided in Table 1. As seen in Fig. 9(a), gas transport is only slightly higher for the metal support, despite a significantly more-open pore structure in com-

Table 3
Morphological properties utilized in anode-functional-layer simulations.

Property	Metallic support	Ni–YSZ AFL
Porosity	41.7%	30%
Mean pore radius (μm)	8.6	0.3
Mean particle diameter (μm)	65	0.3
Catalyst surface area (m^{-1})	0	400,000
Thickness (mm)	1.0	0.03/0.1
Tortuosity	10.1	3.0

parison to the Ni–YRSZ support (Fig. 1). Internal reforming is found to be negligible in the metal support (Fig. 9(b)). Very low H_2 and CO mole fractions are found in the electrolyte-exhaust streams from the metal support, with no flow-rate dependence observed.

Model results are also shown in Fig. 9; these are obtained by setting the active catalyst surface area within the metallic supports to zero. In Fig. 9(a), the model-to-experimental match is good for the CO_2-transport. Hydrogen levels shown for the metal support in Fig. 9(b) are comparable to the H_2 concentration in the forming-gas diluent. This lack of internal reforming in the ITM metallic support motivates development of a Ni–YSZ anode functional layer to be placed atop the ITM support, as described below.

5. Design of anode functional layers for porous-metal supports

To fabricate a complete SOFC, the porous-metallic support is typically coated with thin anode, electrolyte, and cathode layers. The computational model described here can be used to design the anode layer so that adequate internal reforming is realized. Two separate anode functional layers are simulated, with morphological properties listed in Table 3. The porosity, pore radius, and particle diameter are significantly lower for the Ni–YSZ AFLs than for the Ni–YRSZ anode listed in Table 1, reflecting the generally finer pore structure found in anode-functional layers. The catalytically active surface area of the AFLs is also significantly higher than that of the CoorsTek Ni–YRSZ supports. This is possible because of the smaller pore and particle sizes. Internal reforming from two metallic supports with 30 and 100 μm-thick AFLs are compared with that from the bare metallic support, and the CoorsTek Ni–YRSZ support.

For this AFL-design study, models are used to simulate internal steam reforming, rather than the dry-reforming conditions presented previously. For these steam-reforming studies, a 50% H_2O/50% FG mixture is fed to the electrolyte channel, while a 20% CH_4/80% FG mixture is fed to the fuel channel.

The thin anode functional layers are found to have little effect on gas transport through the ITM-alloy supports (results not shown). However, their effect on internal reforming and syngas generation is pronounced. Fig. 10 shows model-predicted electrolyte-side H_2 mole fractions for the bare metallic support, the metallic support with the two different functional layers, and the CoorsTek Ni–YRSZ support. Both the 30-μm AFL and the 100-μm AFL enable significant internal reforming, with approximately 50% more hydrogen generated by the 100-μm-thick AFL. Although the relative level of methane reforming and hydrogen generation by either anode-functional layer remains lower than that of the Ni–YRSZ anode support, syngas formation is clearly much higher in AFL-coated metallic supports than that of the bare metal support.

Fig. 11 shows the H_2-concentration field throughout the metallic support both with and without an AFL at the 75 mL min^{-1} flow rate. Without the AFL (Fig. 11(a)), no hydrogen is generated within the porous metal support, and the 3.5% H_2 present in the forming gas simply diffuses through the metal support, with gradients nearly eliminated over the first 5 mm of the channel. The presence of the AFL results in a far-different H_2 field in Fig. 11(b). Hydrogen is formed at a fairly uniform rate along the length of the channel, with

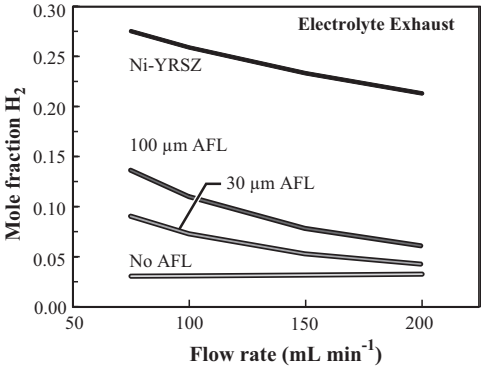

Fig. 10. Model-predicted H_2 mole fractions in the electrolyte-exhaust streams for the ITM metal support equipped with anode functional layers of 30 μm and 100 μm in thickness. Model results for CoorsTek Ni–YRSZ supports and bare ITM supports are also shown for comparison.

facile H_2 diffusion into the the electrolyte channel, and significant diffusion into the metallic support. For the case shown, high CH_4 levels (~6%) are predicted in the electrolyte exhaust, indicating that methane conversion is far from equilibrium in the AFL. Despite this, the anode functional layer enables significant methane conversion and syngas formation in metal-supported SOFCs.

Zhu and Kee [33] have shown that the AFL-morphology can significantly affect the length of the charge-transfer region at the anode-electrolyte interface, with charge-transfer processes extending up to 20 μm from the electrolyte into the AFL. The results shown in Figs. 10 and 11 indicate that a thicker AFL could be beneficial in applications where methane internal reforming is critical.

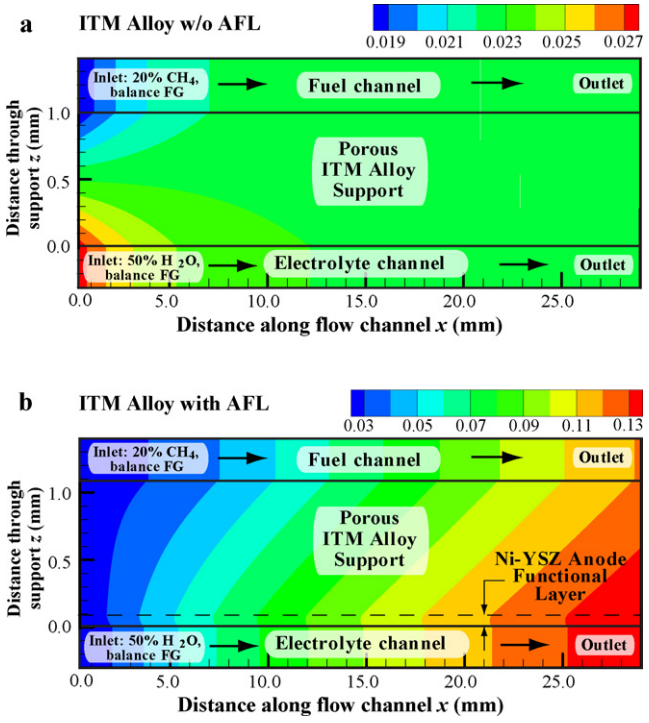

Fig. 11. Contour plots of the H_2 mole fractions within the PLANSEE metal support at the 75 mL min^{-1} flow rate: (a) without anode functional layer; and (b) with a 100 μm-thick Ni–YSZ anode functional layer. Note that the thickness of the metal support (vertical direction) has been scaled by a factor of eight.

6. Conclusions

In this paper, the gas-transport and methane internal-reforming processes of Ni–YSZ and ferritic-steel SOFC supports are compared. The Ni–YSZ supports are fabricated from ceramic powders developed by CoorsTek, Inc. The ferritic-steel supports are provided by PLANSEE SE. Supports are characterized using the unique Separated Anode Experiment that decouples gas-transport and internal-reforming chemistry from electrochemical phenomena. A two-dimensional computational model is utilized to interpret experimental results.

The open pore structure, large pore diameter, and decreased thickness leads to moderately higher gas transport through the ferritic-steel support in comparison to the Ni–YSZ support. However, the PLANSEE support shows virtually no catalytic activity for methane internal reforming, while the Ni–YSZ support is highly active. This lack of internal-reforming in the metallic support motivates the application of the computational model toward design of a Ni–YSZ anode-functional layer (AFL) to be placed atop the metallic support. Model results indicate that anode functional layers enable significant internal reforming and syngas formation, though methane conversion is lower than observed a complete Ni–YSZ anode support. The tools and methods presented here may be used for further design optimization of next-generation SOFC supports and architectures.

Acknowledgements

This work was supported by the Office of Energy Efficiency and Renewable Energy through grant number DE-EE0000260. We gratefully acknowledge Dr. Huayang Zhu and Dr. Andrew Colclasure for assistance in computational-model development. We would also like to thank Sophie Menzer and Dr. Grover Coors of CoorsTek, Inc. for supply of Ni–YRSZ anode-support powders, and Dr. Thomas Franco and Dr. Klaus Rissbacher of PLANSEE SE for supply of porous metallic supports.

References

[1] Y. Lin, Z. Zhan, J. Liu, S.A. Barnett, Solid State Ionics 176 (2005) 1827–1835.
[2] T. Kim, G. Liu, M. Boaro, S.-I. Lee, J.M. Vohs, R.J. Gorte, O.H. Al-Madhi, B.O. Dabbousi, Journal of Power Sources 155 (2006) 231–238.
[3] D.M. Bastidas, S. Tao, J.T.S. Irvine, Journal of Materials Chemistry 16 (2006) 1603–1605.
[4] M. Pillai, I. Kim, D. Bierschenk, S.A. Barnett, Journal of Power Sources 185 (2008) 1086–1093.
[5] M.C. Tucker, Journal of Power Sources 195 (2010) 4570–4582.
[6] T. Franco, K. Schibinger, Z. Ilhan, G. Schiller, A. Venskutonis, ECS Transactions 7 (2007) 771–780.
[7] W. Glatz, G. Kunschert, M. Janousek, 6th European Fuel Cell Forum Proceedings, 2004.
[8] A. Bautista, E. Arahuetes, F. Velasco, C. Moral, R. Calabres, Oxidation of Metals 70 (2008) 267–286.
[9] M. Gazda, P. Jasinski, S. Molin, Solid State Ionics 181 (2010) 1214–1220.
[10] B. Kusz, M. Gazda, P. Jasinski, S. Molin, Journal of Power Sources 181 (2008) 31–37.
[11] L. Rose, O. Kesler, C. Decas-Petit, T. Troczynski, R. Maric, International Journal of Green Energy 6 (2009) 638–645.
[12] M. Rivas, I. Villarreal, N. Burgos, F. Castro, I. Antepara, Journal of Fuel Cell Science and Technology 7 (2010) 061010.
[13] I. Antepara, I. Villareal, L.M. Rodriguez-Martinez, N. Lecanda, U. Castro, A. Laresgoiti, Journal of Power Sources 151 (2005) 103–107.
[14] S. Fontana, R. Amendola, S. Chevalier, P. Piccardo, G. Caboche, M. Viviani, R. Molins, M. Sennour, Journal of Power Sources 171 (2007) 652–662.
[15] H.J. Cho, G.M. Choi, Solid State Ionics 180 (2009) 792–795.
[16] C. Hwang, C.-H. Tsai, C.-H. Lo, C.-H. Sun, Journal of Power Sources 180 (2008) 132–142.
[17] M. Gazda, B. Kusz, P. Jasinski, S. Molin, Journal of the European Ceramic Society 29 (2009) 757–762.
[18] T. Franco, M. Brandner, M. Ruttinger, G. Kunschert, A. Venskutonis, L.S. Sigl, ECS Transactions 25 (2009) 681–688.
[19] D. Storjohann, J. Daggett, N.P. Sullivan, H. Zhu, R.J. Kee, S. Menzer, D. Beeaff, Journal of Power Sources 193 (2009) 706–712.
[20] R. Swartzlander and W.G. Coors. Preparation of yttria-stabilized zirconia reaction sintered products. United States Patent 20070176332 (2007).
[21] E.S. Hecht, G.K. Gupta, H. Zhu, A.M. Dean, R.J. Kee, L. Maier, O. Deutschmann, Applied Catalysis A 295 (2005) 40–51.
[22] J.R. Rostrup-Nielsen, J.-H. Bak Hansen, Journal of Catalysis 144 (1993) 38–49.
[23] E. Mason, A. Malinauskas, Gas Transport in Porous Media: The Dusty-Gas Model, American Elsevier, New York, 1983.
[24] H. Zhu, R.J. Kee, V.M. Janardhanan, O. Deutschmann, D.G. Goodwin, Journal of the Electrochemical Society 152 (2005) A2427–A2440.
[25] R.J. Kee, H. Zhu, D.G. Goodwin, Proceedings of the Combustion Institute 30 (2005) 2379–2404.
[26] G.K. Gupta, E.S. Hecht, H. Zhu, A.M. Dean, R.J. Kee, Journal of Power Sources 156 (2006) 434–447.
[27] R.J. Kee, M.E. Coltrin, P. Glarborg, Chemically Reacting Flow: Theory and Practice, John Wiley, Hoboken, NJ, 2003.
[28] J. Bear, Dynamics of Fluids in Porous Media, American Elsevier, New York, 1972.
[29] S.C. DeCaluwe, H. Zhu, R.J. Kee, G.S. Jackson, Journal of the Electrochemical Society 155 (2008) 538–546.
[30] D.G. Goodwin, In: M. Allendorf, F. Maury, F. Teyssandier (Eds.), The Electrochemical Society, Proceedings Series, vol. 2003-08, 2003, p. 155.
[31] J. Wei, E. Iglesia, Isotopic, Journal of Catalysis 224 (2004) 370–383.
[32] J. Zhu, J.G. van Ommen, L. Leffert, Journal of Catalysis 225 (2004) 388–397.
[33] H. Zhu, R.J. Kee, Journal of the Electrochemical Society 155 (2008) B715–B729.